CrossMark

J. Fluid Mech. (2017), *vol.* 813, *pp.* 412–435. © Cambridge University Press 2017
doi:10.1017/jfm.2016.879

Cross-stream stereoscopic particle image velocimetry of a modified turbulent boundary layer over directional surface pattern

Kevin[1,†], J. P. Monty[1], H. L. Bai[1,2], G. Pathikonda[3,4], B. Nugroho[1], J. M. Barros[3,5], K. T. Christensen[3,4,6] and N. Hutchins[1]

[1]Department of Mechanical Engineering, University of Melbourne, Parkville, Victoria 3010, Australia

[2]Department of Civil and Environmental Engineering, Hong Kong University of Science and Technology, Clear Water Bay, Kowloon, Hong Kong

[3]Department of Mechanical Science and Engineering, University of Illinois at Urbana-Champaign, Urbana, IL 61801, USA

[4]Department of Aerospace and Mechanical Engineering, University of Notre Dame, Notre Dame, IN 46556, USA

[5]Department of Mechanical Engineering, United States Naval Academy, Annapolis, MD 21402, USA

[6]International Institute for Carbon Neutral Energy Research (WPI-I^{2}CNER), Kyushu University, Fukuoka 819-0395, Japan

(Received 8 August 2016; revised 12 December 2016; accepted 16 December 2016; first published online 23 January 2017)

A turbulent boundary layer developed over a herringbone patterned riblet surface is investigated using stereoscopic particle image velocimetry in the cross-stream plane at $Re_\tau \approx 3900$. The three velocity components resulting from this experiment reveal a pronounced spanwise periodicity in all single-point velocity statistics. Consistent with previous hot-wire studies over similar-type riblets, we observe a weak time-average secondary flow in the form of δ-filling streamwise vortices. The observed differences in the surface and secondary flow characteristics, compared to other heterogeneous-roughness studies, may suggest that different mechanisms are responsible for the flow modifications in this case. Observations of instantaneous velocity fields reveal modified and rearranged turbulence structures. The instantaneous snapshots also suggest that the time-average secondary flow may be an artefact arising from superpositions of much stronger instantaneous turbulent events enhanced by the surface texture. In addition, the observed instantaneous secondary motions seem to have promoted a free-stream-engulfing behaviour in the outer layer, which would indicate an increase turbulent/non-turbulent flow mixing. It is overall demonstrated that the presence of large-scale directionality in transitional surface roughness can cause a modification throughout the entire boundary layer, even when the roughness height is 0.5 % of the layer thickness.

Key words: boundary layer structure, turbulence control, turbulent boundary layers

† Email address for correspondence: kevin.kevin@unimelb.edu.au

https://doi.org/10.1017/jfm.2016.879 Published online by Cambridge University Press

1. Introduction

Streamwise-aligned riblets as a means of passively controlling wall-bounded turbulent flows have been well studied. Their ability to reduce the skin-friction drag has been reported by numerous researchers (Choi 1989; Walsh 1990; Bechert *et al.* 1997; Bechert, Bruse & Hage 2000; García-Mayoral & Jiménez 2011, to name a few), and the ribs' near-wall stabilising mechanisms are discussed by Bechert & Bartenwerfer (1989), Choi (1989), Luchini, Manzo & Pozzi (1991). A bio-inspired riblet alignment was later introduced by Koeltzsch, Dinkelacker & Grundmann (2002), where the ribs are arranged in a converging and diverging (hereafter abbreviated as C–D) pattern. A converging texture is often observed upstream of sensory receptors on fast swimming sharks, and diverging texture is commonly observed around the lateral-line organs. This C–D pattern was tested by Koeltzsch *et al.* (2002) in a fully turbulent pipe flow, where one half of the inner surface of the pipe was covered with ribs which were yawed at -45° to the axial direction, and the other half at $+45^\circ$. From their hot-wire experiments, Koeltzsch *et al.* (2002) observed a large azimuthal variation in the flow statistics. Above the line of flow convergence, the local mean axial velocity was lower, coupled with an increase in turbulence intensity. Above the region of flow divergence however, the opposite scenarios occurred. The C–D riblet pattern was later implemented in a turbulent boundary layer by Nugroho, Hutchins & Monty (2013), where they found higher/lower streamwise momentum deficit (hence a thicker/thinner local boundary layer) over the converging/diverging region respectively. They also characterised several parameters which affect the magnitude of this spanwise flow variation. From their mean-flow mapping using a hot-wire probe, they show that the rib's yaw angle, viscous-scaled rib height and the flow development length over the C–D surface, affect the extent of boundary layer modification. A follow up study by Nugroho *et al.* (2014) later indicated that this spanwise periodicity is also accompanied by time-average δ-scale streamwise roll modes. Relying on the spectrogram of streamwise velocity fluctuations, it was speculated that the C–D pattern might preferentially arrange the naturally occurring very-large-scale motions that are prevalent in wall-bounded turbulence (Kim & Adrian 1999; Adrian, Meinhart & Tomkins 2000*b*; del Álamo *et al.* 2006; Hutchins & Marusic 2007; Monty *et al.* 2007).

Time-average streamwise roll modes, commonly referred as the mean secondary flows, have also been identified in many recent studies over various surface roughness and topographies. To give a few examples, they are observed in open water channel flows over spanwise alternating smooth and rough bedforms (Wang & Cheng 2006), in turbulent boundary layers over spanwise-periodic obstacles aligned in the flow direction (Vanderwel & Ganapathisubramani 2015), over complex realistic roughness replicated from a damaged turbine blade (Barros & Christensen 2014) and also over spanwise alternating regions of wall drag (large-eddy simulation study by Willingham *et al.* 2014). It is a challenge to explain the physical mechanisms of how these time-average secondary flows arise. Anderson *et al.* (2015) analyse the aforementioned simulation results as well as the experiment over the complex turbine roughness, and attribute the occurrence of the time-average secondary flow to the uneven distribution of Reynolds stresses (following the turbulence kinetic energy balance approach of Hinze (1967)).

The aim of the current study is to investigate how the turbulence structures behave under the deliberately triggered secondary flow over the C–D riblets, based on instantaneous particle image velocimetry (PIV) fields in the orthogonal cross-stream plane. The large field-of-view (FOV) measurement is designed to capture the full

https://doi.org/10.1017/jfm.2016.879 Published online by Cambridge University Press

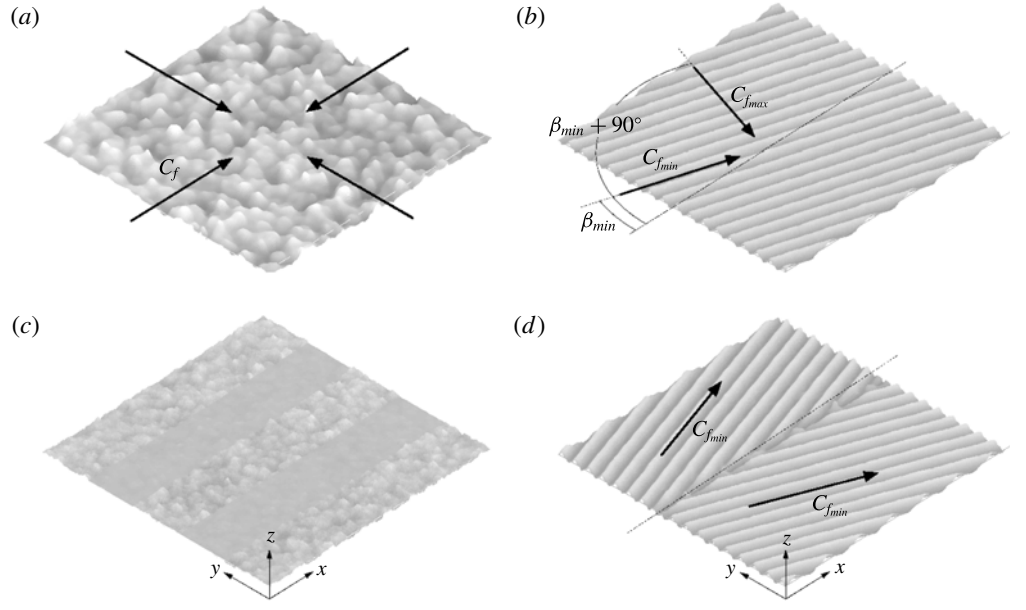


FIGURE 1. Comparison between surface topography with locally isotropic/anisotropic C_f, in spanwise homogeneous/heterogeneous distribution. Refer to table 1 for the surface category.

Figure 1	Local C_f isotropy	C_f distribution
(*a*)	Isotropic	Homogeneous
(*b*)	Anisotropic	Homogeneous
(*c*)	Isotropic	Heterogeneous
(*d*)	Anisotropic	Heterogeneous

TABLE 1. Type of surface roughness categorised in figure 1.

extent of the largest-scale modified structures. The single-point velocity statistics will also be discussed briefly to support and complement previous observations of Nugroho *et al.* (2013). The PIV snapshots offer a more detailed view of the instantaneous events that give rise to the time-average secondary flows previously observed over this herringbone pattern. Here the axis system x, y and z refer to the streamwise, spanwise and wall-normal directions, with u, v and w indicating the respective total velocity components.

2. Surface roughness

2.1. *Surface roughness classification*

There are endless rough surface topographies and arrangements that are present in nature and engineering. To date, the focus has been on the local roughness distributions and their effects on the flow. One convenient way to characterise roughness geometry is by its equivalent sand grain roughness height k_s (Perry, Schofield & Joubert 1969; Jiménez 2004), which is effectively a measure of the

https://doi.org/10.1017/jfm.2016.879 Published online by Cambridge University Press

roughness' influence on the flow. Many physical attributes of the surface topography have been suggested to influence k_s including (but not limited to) solidity, effective slope, skewness and average height (Acharya, Bornstein & Escudier 1986; Napoli, Armenio & Marchis 2008; Flack & Schultz 2010; Chan *et al.* 2015). Perhaps the most relevant roughness characterisation to this study is the ability of certain surfaces to induce large-scale secondary motions to the base flow, as is commonly observed over spanwise heterogeneous roughness (Hinze 1967; Wang & Cheng 2006; Vermaas, Uijttewaal & Hoitink 2011; Mejia-Alvarez & Christensen 2013; Barros & Christensen 2014; Willingham *et al.* 2014; Vanderwel & Ganapathisubramani 2015). However, it is important to recognise that the surface that we are studying here differs to those listed above, in the sense that it exhibits both large-scale spanwise heterogeneity (roughness characteristics that vary as a function of y) and directionality or anisotropy (a wall drag that depends on flow direction). To illustrate this distinction, figure 1 and the accompanying table show examples of surfaces under varying states of homogeneity and isotropy. To be clear, when we refer to heterogeneity or anisotropy, we refer to variations or directionality in roughness properties occurring over a wall-parallel length-scale that is $\gg k_s$ and some appreciable proportion of the layer thickness.

Figure 1(a) shows an example of an isotropic-homogeneous roughness which is represented by a sandpaper surface. A change in the instantaneous flow direction over this locally isotropic roughness causes no definite change in the skin-friction coefficient C_f. In addition, the wall-drag distribution is homogeneous over this surface (i.e. is not a function of x and y location). To date, most engineering and meteorological surfaces are assumed to fall within this category, and indeed it is only for this roughness category that current tools permit full-scale predictions. This is usually obtained via the Moody chart for fully developed pipe flow (Moody 1944; Shockling, Allen & Smits 2006) or developments for the zero-pressure-gradient flat plate turbulent boundary layer (Prandtl & Schlichting 1955; Granville 1958). Figure 1(b) displays an example of an anisotropic (directional)-homogeneous roughness which is represented by a standard riblets profile. As illustrated by this figure, a different instantaneous flow direction β will yield a different value of C_f. The minimum C_f over the riblets will be obtained where the local flow direction is parallel with the grooves, and it will increase systematically with the yaw angle, to reach a maximum value when the motion is perpendicular to the grooves. The minimum/maximum resistance was examined by Luchini *et al.* (1991) using Stokes flow analysis, where they show the deeper/shallower protrusion heights for flow parallel/across the grooves. The anisotropy in skin-friction coefficient was also demonstrated by Walsh (1990) who studied the dependence of riblets drag reduction with yaw angle. Similar to figure 1(a), the wall-drag distribution for this grooved surface is homogeneous though for a given flow direction. Transverse bars studied by Volino, Schultz & Flack (2009), honed pipes investigated by Shockling *et al.* (2006) or even wind over the ocean waves will also fit within this category.

Figure 1(c) gives an example of a surface with spanwise heterogeneity. The roughness is arranged in spanwise-alternating strips of varying roughness height. For flow in the x direction, this surface is known to give rise to secondary flows centred about the step change of the wall drag (Hinze 1967; Wang & Cheng 2006; Willingham *et al.* 2014). Note that although this surface has a degree of directionality (in the sense that it will perform quite differently when the flow is in the y direction, hence it becomes a streamwise heterogeneous roughness), the individual roughness patches are locally isotropic. This is because the surface shown in figure 1(c) is comprised of sandpaper-type roughness. Therefore, we classify

https://doi.org/10.1017/jfm.2016.879 Published online by Cambridge University Press

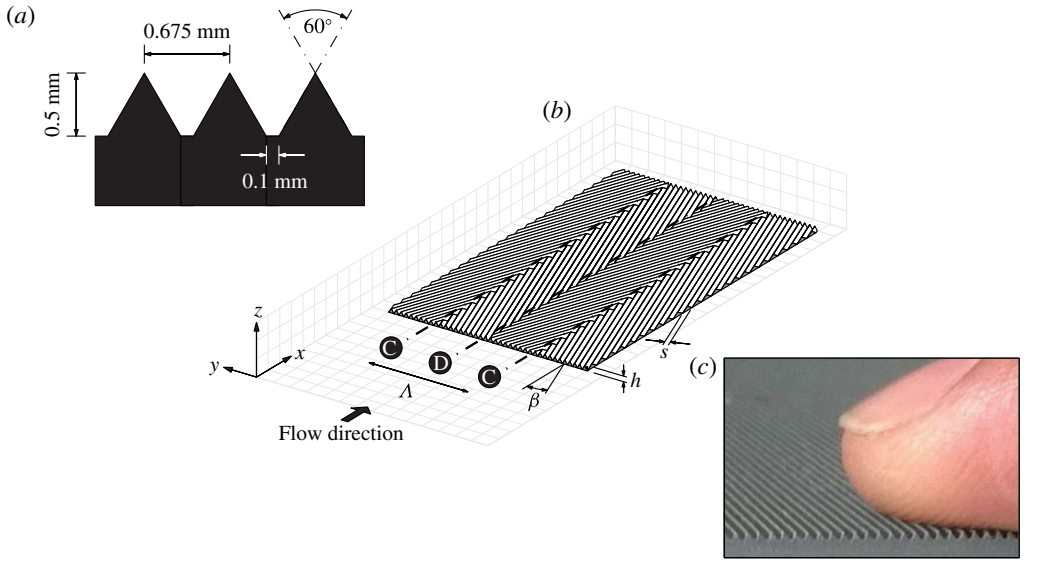


FIGURE 2. (Colour online) (*a*) Ribs cross-section. (*b*) Schematic drawing of the C–D riblets, showing several key parameters. (*c*) Picture of the actual riblet grooves.

this surface as isotropic heterogeneous. Rivet rows on an aircraft fuselage that are commonly streamwise-aligned, spanwise-alternating river bedforms such as those studied by Wang & Cheng (2006), and even the edges of forests under the atmospheric surface layer are examples of this surface type. Note that this isotropic-heterogeneous arrangement can also be formed in a more irregular manner than the example given in figure 1(*c*). This is demonstrated by the turbine blade roughness studied by Barros & Christensen (2014) that produces distinct mean streamwise vortices above the surface, which are attributed to the large-scale (spanwise) topography variation that is present within the roughness complexity. Finally, figure 1(*d*) shows an anisotropic surface that also has a large-scale heterogeneity in the form of a spanwise-varying directional roughness. This surface closely resembles the pattern surrounding the sharks' lateral-line organ (Koeltzsch *et al.* 2002) and also that found on the feathers of birds (Chen *et al.* 2014). Note that the minimum-C_f vectors drawn represent the local direction of least resistance on this anisotropic surface. However, the study of Nugroho *et al.* (2013) over a similar pattern indicates that the mean streamwise wall drag is a complex function of spanwise location y. Furthermore, large-scale secondary motion following a highly modified boundary layer is observed. In this paper we will further investigate how this anisotropic-heterogeneous surface produces such profound modifications to the turbulent boundary layer, despite having a small k/δ.

2.2. *Converging–diverging riblets*

The directional-heterogeneous roughness under study is a converging–diverging riblet arrangement similar to that originally fabricated and studied by Nugroho *et al.* (2013). It consists of a repeating pattern of alternating converging and diverging grooves arranged in a 'herringbone-type' pattern. Figure 2 is a schematic drawing of the riblet surface defining several key parameters. The height of each rib $h = 0.5$ mm and the spacing $s = 0.68$ mm, giving $h^+ = hU_{\tau s}/\nu \approx 18$ and $s^+ = sU_{\tau s}/\nu \approx 24$ (where

https://doi.org/10.1017/jfm.2016.879 Published online by Cambridge University Press

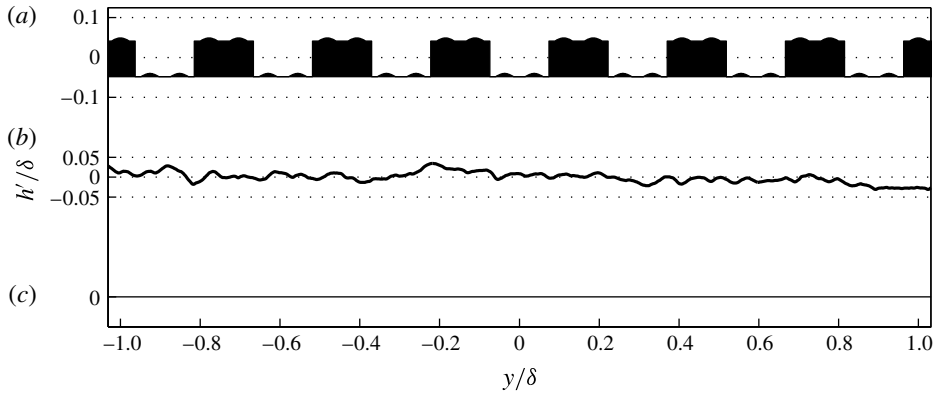


FIGURE 3. Comparison of the spanwise-profile surface topographies (about their mean elevation height) averaged over δ-long streamwise fetch, between the study of (*a*) Vanderwel & Ganapathisubramani (2015), (*b*) Barros & Christensen (2014) and (*c*) current study.

$U_{\tau s}$ is the smooth-wall friction velocity at the same inflow condition). At the present streamwise location, the rib height yields a blockage ratio of $h/\delta_s \approx 0.005$ (where δ_s is the smooth-wall boundary layer thickness). As shown in figure 2(*a*), the cross-section of the ribs represents a trapezoidal profile. This shape is the consequence of the 0.1 mm flat-chamfered tip of the 60° cutter that was used to groove the surface. The ribs are yawed at an angle $\beta = \pm 20°$ from the main flow direction to create regions of convergence and divergence. The width of each converging/diverging region is 73.75 mm, giving a repeating C–D wavelength of $\Lambda = 147.5$ mm (or $\Lambda/\delta_s \approx 1.5$). Note that the schematic drawing of figure 2(*b*) is not drawn to scale, where in reality one complete C–D wavelength Λ consists of more than 200 yawed ribs. Figure 2(*c*) gives a sense of the actual rib dimensions.

2.3. *Does spanwise variation of wall drag cause the boundary layer modification over the converging–diverging riblets?*

As previously discussed, a spanwise C_f heterogeneity has been shown to give rise to secondary motions in the boundary layer. A recent paper by Anderson *et al.* (2015) addresses the qualitative flow similarity between the simulation by Willingham *et al.* (2014) and the flow observed over the surface of Barros & Christensen (2014). In all cases, they suggest that the wall-drag variation gives rise to the generation of the observed secondary flows, by creating an imbalance in the Reynolds stress distribution. A study by Vanderwel & Ganapathisubramani (2015) also concludes that large-scale variation in surface elevation, which translates to varying aerodynamic wall drag, is able to produce a mean secondary flow (although it is noted that their mean secondary flows turn in an opposite sense to those listed above, with common flow up over the elevated regions). Over the C–D riblets studied here, spanwise variations of wall drag are also observed accompanying a highly modified boundary layer (see Nugroho *et al.* 2013). However, it is wise to be cautious in aligning the C–D riblet surface to the spanwise heterogeneous roughness listed above. Figure 3 puts this issue into perspective. It compares the spanwise surface profiles of (*a*) Vanderwel & Ganapathisubramani (2015), (*b*) Barros & Christensen (2014) and (*c*)

https://doi.org/10.1017/jfm.2016.879 Published online by Cambridge University Press

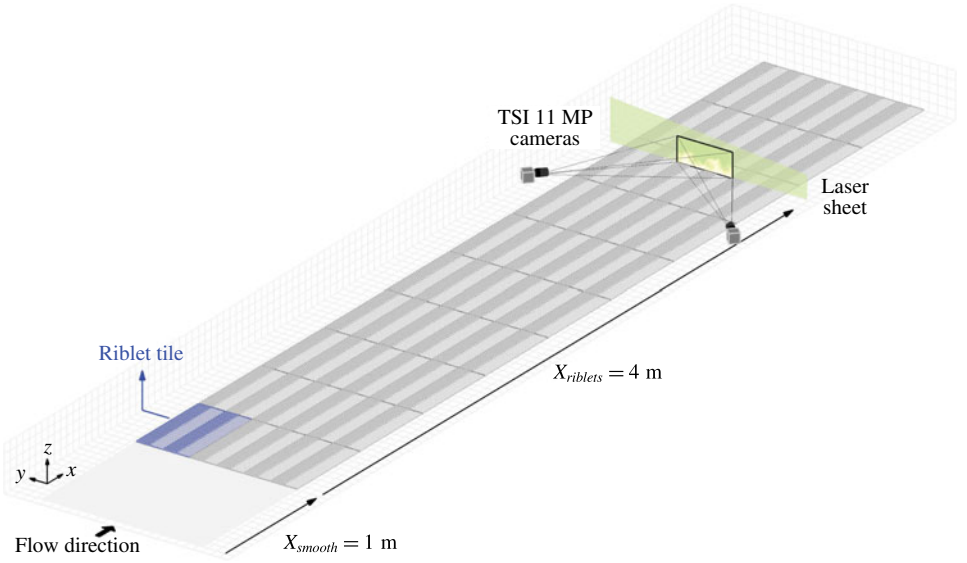


FIGURE 4. (Colour online) Schematic drawing of the stereoscopic PIV set-up, showing the surface configuration, laser sheet direction and camera arrangement.

the current study, averaged over a δ-long streamwise fetch. This streamwise averaging of surface topography was previously used by Barros & Christensen (2014) to provide a qualitative representation of the imposed aerodynamic drag. In other words, the wall drag is higher when the profile is protruding, and is lower when the profile is recessed. Looking at figure 3(*a*,*b*), we can clearly see the variation in the surface height characterised as a spanwise heterogeneous surface. Over the C–D riblets however, there is no variation in the elevation over this streamwise-averaged profile, or $h \neq f(y)$. Even if we do not streamwise average the C–D riblet topography, the cross-sectional profile will simply look like a regular rib (e.g. sawtooth/blade/trapezoidal) texture. The only thing that varies over the spanwise wavelength of the C–D pattern is the direction of the minimum/maximum flow resistance (Luchini *et al.* 1991). Hence, it would appear that the anisotropy or directionality in the C–D riblets may play a key role. Therefore, we should remain open to the possibility that different driving mechanisms might be responsible for generating the mean secondary flow in the C–D riblet case.

3. Stereoscopic PIV experiments

The cross-stream plane stereoscopic PIV (sPIV) experiments are conducted in an open return suction-type wind tunnel at the University of Illinois at Urbana-Champaign. The wind tunnel has a working section of $6 \times 0.91 \times 0.46$ m. The characteristics of this tunnel have been documented in many past studies (Adrian *et al.* 2000*b*; Tomkins & Adrian 2003; Wu & Christensen 2010). Both the riblets and smooth-wall base-case experiments are conducted at a streamwise location of $x = 5$ m at nominal free-stream velocity of 17.0 ms^{-1}. Both cases are performed under zero-pressure-gradient conditions. Figure 4 presents a schematic drawing of the sPIV set-up. For the riblet measurement, the boundary layer is first developed over a smooth wall for 1 m, then transitioned (with the crest of the riblets levels with

https://doi.org/10.1017/jfm.2016.879 Published online by Cambridge University Press

the upstream smooth wall) and developed over the C–D riblets for 4 m. The C–D riblets were manufactured as a set of textured tiles made from polyurethane cast, with each tile having the dimension of 515 × 300 mm. The readers are referred to Nugroho *et al.* (2013) for full details of the manufacturing technique. Additionally, the riblet surface is dyed black at the measurement location using polymeric colourant to reduce background reflection in the PIV images. A total of 30 riblet tiles are used to cover the floor of the wind tunnel working section, covering the entire spanwise width with three tiles, equivalent to six complete C–D wavelengths Λ.

The flow is seeded with 1 μm olive oil droplets generated using 15 Laskin nozzle arrays, and illuminated with a 2 mm thick laser sheet generated by a dual-cavity 190 mJ per pulse Nd:YAG laser (Quantel) and a series of cylindrical lenses. The laser sheet enters the plane of interest from the side of the tunnel, which further minimises the frontal light reflection issuing from the riblet surface. The imaging system is two TSI 11MP cameras (4000 × 2672 pixels, 12-bit frame-straddled CCD) equipped with Sigma 180 mm macro lenses. The cameras view the cross-flow plane through optical-grade glass side walls at an upstream angle of ±45° from the streamwise direction. Uniform image focus is obtained across the entire FOV by satisfying the Scheimpflug condition. To observe the full extent of the largest-scale modified structures, a wide FOV in spanwise-wall-normal domain of $3.1 \times 1.5\delta_s$ is captured, which spans approximately two complete C–D wavelengths. The stereoscopic calibration images are taken using a single-plane target (covering $2.8 \times 1.5\delta_s$) taken at five x-locations with 250 μm separation. The mapping functions from the two-dimensional image space to the three-dimensional real space are computed using a least-squares polynomial with cubic dependence in the in-plane directions and linear in the out-of-plane direction. The derivatives of these mapping functions are used to reconstruct the three velocity components from the particle pixel displacements (which are computed in the warped image) based on the method proposed by Soloff, Adrian & Liu (1997). The pixel displacements are processed using an in-house PIV package, where the details of the processing algorithm are available in de Silva *et al.* (2014). A final interrogation window size of 16 × 16 pixel with 50 % overlap is employed. Since the velocity vectors are computed with a fixed interrogation window size throughout the entire image, the variation in the camera magnification due to perspective view results in the gradation of the spatial resolution, with the range of 93 μm pixel^{-1} ±15 % in spanwise direction and 66 μm pixel^{-1} ±10 % in wall-normal direction. Together with the laser-sheet thickness, these values yield a mean (viscous-scaled) interrogation spot size of $\Delta x^+ \times \Delta y^+ \times \Delta z^+ = 77 \times 57 \times 40$ for the smooth-wall base-case flow. Seven thousand three-component instantaneous velocity realisations are taken for the riblets case and 2500 for the smooth-wall case. An acquisition rate of 0.5 Hz is employed to ensure statistical independence, which is equivalent to approximately 350 boundary layer turn over times between consecutive snapshots.

To assess the quality of the experiments, a smooth-wall boundary layer measurement at lower Reynolds number of $Re_\tau = 2560$ (at the same streamwise location, with lower free-stream velocity of $U_\infty = 10.9$ m s^{-1}) is also performed. This dataset allows a direct comparison to the existing boundary layer simulation of Eitel-Amor, Örlü & Schlatter (2014) at comparable Reynolds number of $Re_\tau = 2479$. Figure 5(*a*) shows the viscous-scaled mean streamwise velocity profile for the validation case. For clarity of presentation, the data points are down sampled to 30 wall-normal locations spaced logarithmically. A good collapse with the reference profile of Eitel-Amor *et al.* (2014) is clearly evident throughout the boundary layer. Figure 5(*a*,*b*) also

https://doi.org/10.1017/jfm.2016.879 Published online by Cambridge University Press

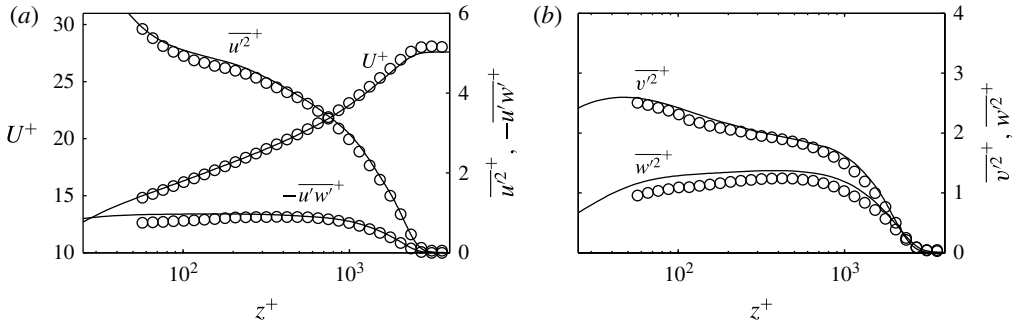


FIGURE 5. Validation of sPIV statistics performed on the smooth wall at $Re_\tau = 2560$. The second-order statistics are corrected using the method proposed by Lee *et al.* (2016) to account for the spatial attenuation due to finite PIV interrogation volume. Solid lines are reference statistics taken from simulation data of Eitel-Amor *et al.* (2014) at $Re_\tau = 2479$.

Surface	Re_θ	U_∞ (m s^{-1})	δ (mm)	FOV ($\delta \times \delta$)	Number of realisations
Smooth (validation)	8 000	10.9	99.3	3.1 × 1.5	2500
Smooth (base case)	12 300	16.7	96.2	3.2 × 1.5	2500
C–D riblets	13 000	17.0	99.6	3.1 × 1.4	7000

TABLE 2. Experimental parameters of the current sPIV experiments.

presents the Reynolds stress profiles. Note that these second-order statistics have been corrected using a method proposed by Lee *et al.* (2016), to account for the spatial attenuation due to volume averaging inherent in PIV interrogation. This method essentially approximates the reduction in turbulence intensity profiles due to small-scale unresolved energy, simply given the finite interrogation volume size in viscous units. Despite the slight underestimation that remains in these fluctuation statistics, which may result from the spatial-resolution variation across the wide FOV, the facility and measurement system clearly yield the expected velocity statistics at this moderate Reynolds number.

The experimental conditions as well as the PIV parameters are summarised in table 2. Note that for the C–D riblets case, since parameters such as δ and θ (hence Re_θ) are functions of spanwise location y, the values presented in the table correspond to the spanwise-averaged value over one complete C–D wavelength $\langle\cdot\rangle_\Lambda$. Here δ or $\delta(y)$ corresponds to the wall distance where the mean streamwise velocity reaches 99 % of the free-stream velocity. To highlight the physical modifications caused by the C–D riblets with respect to the smooth-wall base case, the ordinate of the velocity maps are normalised by the smooth-wall boundary layer thickness δ_s throughout this paper. The abscissa however, are normalised by the C–D wavelength Λ while maintaining the physical aspect ratio. Here the diverging region is located at $y/\Lambda = 0$ and converging region at $y/\Lambda = \pm 0.5$ (indicated by the Ⓓ and Ⓒ symbols respectively). All velocities are normalised by the corresponding free-stream velocity U_∞. The flow direction in all the velocity maps presented is out of the page.

https://doi.org/10.1017/jfm.2016.879 Published online by Cambridge University Press

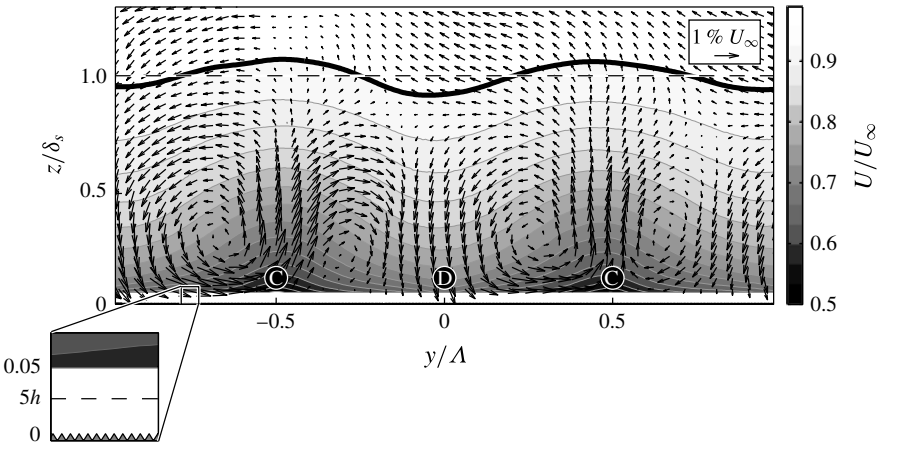


FIGURE 6. Contours of time-average streamwise velocity normalised by the free-stream velocity U/U_∞ over the C–D riblets. The time-average in-plane velocity vectors V and W are superimposed. Solid line: local boundary layer thickness δ; dashed line: spanwise-averaged boundary layer thickness $\langle\delta\rangle_\Lambda$. Inset highlights the rib height.

4. Velocity statistics and decomposition

4.1. *Mean velocity field*

Figure 6 shows contours of time (ensemble)-averaged streamwise velocity over the C–D riblets. Thick black contour line indicates the local boundary layer thickness $\delta(y)$, and its spanwise-averaged value $\langle\delta\rangle_\Lambda$ is shown by the dashed line. Despite having groove heights of $h/\delta_s \approx 0.005$ as indicated by the inset, pronounced spanwise periodicity induced by the C–D pattern is clearly displayed in figure 6. The mean streamwise velocity is much lower near the converging region compared to the diverging at a given wall height. This variation in momentum defect extends up to the edge of the boundary layer resulting in a periodicity in the local δ, which is approximately $\pm 8\,\%$ of its spanwise-averaged value $\langle\delta\rangle_\Lambda$. In some sense, this observation challenges the classical-roughness assumption which states that the roughness height needs to be at least of order $h/\delta \approx 1/40$ before its influence extends across the entire layer (Jiménez 2004). However, it is important to recognise that the present surface exhibits anisotropy as well as spanwise C_f heterogeneity. Spanwise heterogeneity in roughness height (figure 1*c*) could also cause a similar scenario. In both cases, the wavelength of the heterogeneity seems to play a strong role in how far the three-dimensionality observed in the flow extends from the wall (see for example coarse- and fine-spaced results from Vanderwel & Ganapathisubramani 2015).

Similar mean streamwise velocity behaviour was previously shown by Nugroho *et al.* (2013) from the hot-wire flow mapping over the same type of riblets. They also attempted to approximate the wall drag over the line of convergence and divergence using the local velocity profiles. From both the modified-Clauser (Perry & Li 1990) as well as the momentum-integral method (Anders 1990), they found that the converging pattern increases the wall drag (with respect to the smooth-wall comparison) whilst the diverging pattern reduces the drag. In this experiment, we found a similar wall-drag behaviour from three different estimation methods, namely modified-Clauser, momentum-integral and the total-shear-stress method (Flack, Schultz & Shapiro 2005). From these methods we tentatively estimate the drag increase over

https://doi.org/10.1017/jfm.2016.879 Published online by Cambridge University Press

the converging region to be ∼30 % and the drag decrease over the diverging to be ∼20 %. Furthermore, recent pipe flow experiments by Chen *et al.* (2014) obtained significant total drag reductions over similar herringbone riblets (based on the changes in the pressure gradient), by replacing the converging regions with strips of smooth surface. This strategy works perhaps by negating the drag increase induced by the converging region, while still exploiting the drag reducing property of diverging riblet pattern. Therefore, in the absence of a direct wall-drag measure, we label the converging/diverging region as the region of higher/lower wall drag respectively, based on the aforementioned approximation techniques and consistent with the results of Chen *et al.* (2014).

The accompanying time-averaged in-plane velocity vectors V and W are also visualised in figure 6. The plot shows the existence of δ-filling counter-rotating roll modes in the mean field centred at $z/\delta_s \approx 0.3$. The maximum mean vertical motion captured within this field of view is $W \approx 1.5\,\%$ of U_∞. The vectors also confirm that the mean common flow up occurs above the converging (higher wall-drag) region and mean common flow down occurs above the diverging (lower wall-drag) region. Periodic mean secondary flows are also observed over spanwise heterogeneous roughness tested by Wang & Cheng (2006) and in simulation results analysed by Anderson *et al.* (2015). Interestingly, the sign of their streamwise vortices is the opposite of the one shown in the present study. They observed a mean common flow down over the higher drag region. It was noted by Hinze (1973) however, that the rotational direction over this type of heterogeneous drag/roughness patches are not imperative. Depending on the roughness configuration, either common flow up or down can occur over the rougher patch. For the case of secondary flow observed by Vanderwel & Ganapathisubramani (2015), the rotational sense seems to be similar to the current study (upward motion over the higher drag region). However, the results of Vanderwel & Ganapathisubramani (2015) could be viewed more as spanwise changes in surface elevation rather than heterogeneous roughness. All these differences suggest that different driving mechanisms might be responsible for generating the mean secondary flow in each case. The orientation of the currently observed mean roll modes can be determined from a consideration of the direct influence of the ribs to the shear flow above them. The yawed riblets impose lesser/greater flow resistance in the direction parallel/misaligned to the grooves (Luchini *et al.* 1991), or alternatively, modify the forward mobility tensor as proposed by Kamrin, Bazant & Stone (2010).

4.2. *Velocity decomposition*

Due to the spanwise periodicity present in the boundary layer, there is an opportunity to apply a triple decomposition to the velocity results. The total velocity in the cross-stream plane can be decomposed into,

$$u_i(y,z,t) = U_i(y,z) + u_i'(y,z,t) \tag{4.1a}$$

$$= \langle U_i \rangle_\Lambda(z) + \widetilde{U}_i(y,z) + u_i'(y,z,t) \tag{4.1b}$$

$$= \langle U_i \rangle_\Lambda(z) + \widetilde{u}_i'(y,z,t). \tag{4.1c}$$

This method of decomposition is commonly used in analysing flows over plant canopies where the rough surfaces are spatially inhomogeneous (Raupach & Shaw 1982; Finnigan 2000; Coceal *et al.* 2006). Figure 7 illustrates this decomposition. The total velocity u_i can be temporally/Reynolds decomposed into U_i, which is the time-averaged mean velocity (also known as the local mean) and u_i' which is the

https://doi.org/10.1017/jfm.2016.879 Published online by Cambridge University Press

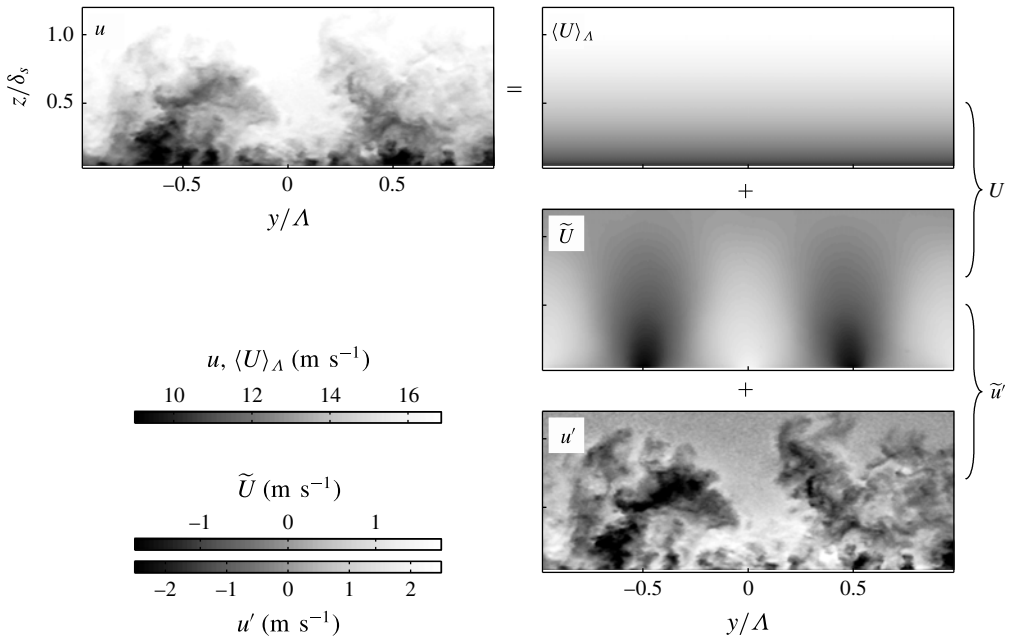


FIGURE 7. Example of total streamwise velocity field u over the C–D riblets, triply decomposed into the global mean $\langle U\rangle_\Lambda$, non-convecting spatial variation $\widetilde{U}$ and temporal/convecting fluctuation u'.

turbulence (convecting) fluctuations about the time-averaged values. For the present surface, U_i will be a function of y and z, reflecting the spanwise variation observed in figure 6. $\langle U_i\rangle_\Lambda$ is the spatially and temporally averaged mean velocity (also known as the global mean) taken by averaging U_i over one complete C–D wavelength. $\widetilde{U}_i = U_i - \langle U_i\rangle_\Lambda$ is the spanwise variation of the time-averaged velocity. This term represents the spatial time-invariant variation of the flow, due to the more frequent occurrence of lower-/higher-speed fluid over the converging/diverging part of the riblets respectively. The non-zero values of this term add dispersive stress components $\langle\widetilde{U}_i\widetilde{U}_i\rangle_\Lambda$ to the stress tensor, which represent the additional transport of momentum by spatial flow variation in the spanwise direction (Coceal *et al.* 2006). From (4.1*c*), $\widetilde{u}'$ is the combination of the non-convecting spatial variation $\widetilde{U}$ and the convecting turbulence fluctuation u'. Therefore, under this spatio-temporal decomposition, the converging region will most likely have negative $\widetilde{u}'$ values close to the surface where the amplitude of the alternating positive/negative $\widetilde{U}$ is most pronounced.

The difference between the two decomposition methods (4.1*b*) and (4.1*c*), also appears in the single-point velocity statistics. Figure 8(*a*,*b*) compares the streamwise and wall-normal turbulence intensities computed using both temporal fluctuation u_i' (open symbol) and spatio-temporal fluctuation $\widetilde{u}_i'$ (closed symbols). These profiles are taken above the converging line at $y/\Lambda = 0.5$. The smooth-wall profiles are also included as the solid lines for comparisons. The abscissa of this figure are normalised by the local boundary layer thickness δ for scaling purposes, and the ordinate by the corresponding U_∞. Figure 8(*a*) clearly shows that the variance computed about the global mean $\overline{\widetilde{u}'^2}$ is higher, with an intensity of more than three times of $\overline{u'^2}$ at the measurement point closest to the surface. For the wall-normal velocity component

https://doi.org/10.1017/jfm.2016.879 Published online by Cambridge University Press

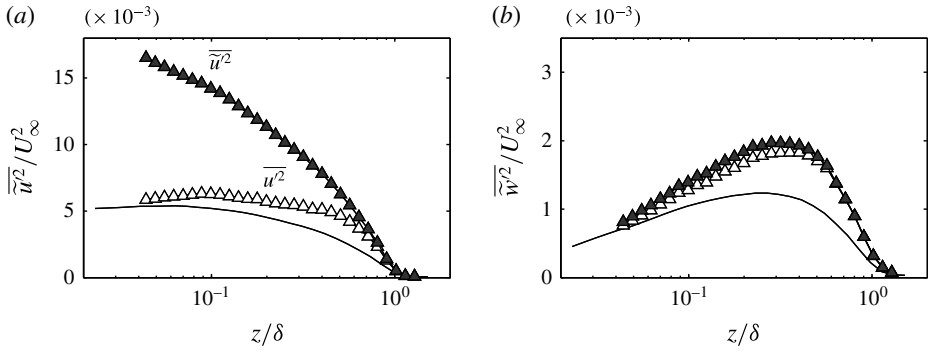


FIGURE 8. Streamwise (*a*) and wall-normal (*b*) turbulence intensity profile over the converging (symbols) region and smooth-wall reference (−). △: Profile computed from Reynolds (convecting) fluctuation u'; and ▲: from spatio-temporal fluctuation $\widetilde{u}'$. Spatial-resolution correction is not applied in this figure.

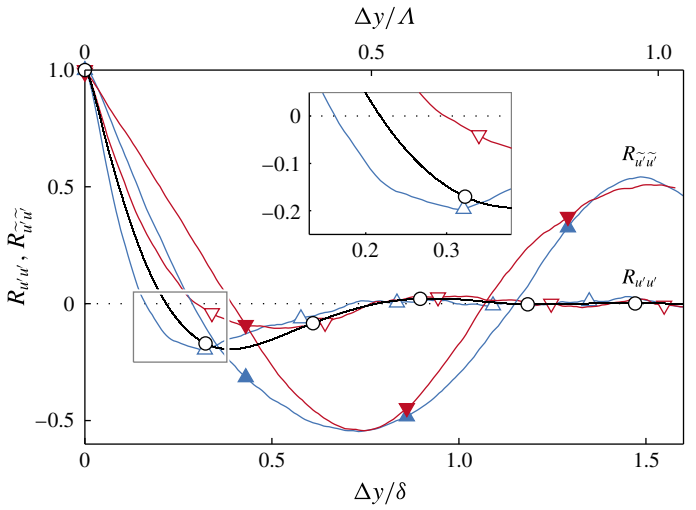


FIGURE 9. (Colour online) Spanwise slices through fluctuations self-correlation points at $z_{ref}/\delta = 0.15$ over converging region (▲, blue and △, blue), diverging region (▼, red and ▽, red), and smooth wall (○). Open symbols: profiles computed using temporal fluctuations $R_{u'u'}$. Closed symbols: profiles computed using spatio-temporal fluctuation $R_{\widetilde{u}'\widetilde{u}'}$.

however, since the time-averaged spatial variation $\widetilde{W}$ is very weak (and zero for $\widetilde{V}$ due to symmetry), the additional energy contribution from this time-invariant mode is insignificant. This is indicated by the minor difference in the wall-normal variances computed using the two different fluctuations. The effect of subtracting global/local mean also appears in spatial statistics such as the two-point velocity correlation. Figure 9 presents the correlation coefficient of streamwise velocity fluctuation, where all the profiles are computed about $z_{ref}/\delta(y) = 0.15$ over the converging, diverging and the smooth-wall reference case. When the correlation is calculated using the fluctuations about the global mean $\widetilde{u}'$, a clear ringing effect with the wavelength corresponding to Λ is observed in $R_{\widetilde{u}'\widetilde{u}'}$. This is expected due to the occurrence of the positive/negative $\widetilde{u}'$ over the riblets. When only considering the convecting turbulence

https://doi.org/10.1017/jfm.2016.879 Published online by Cambridge University Press

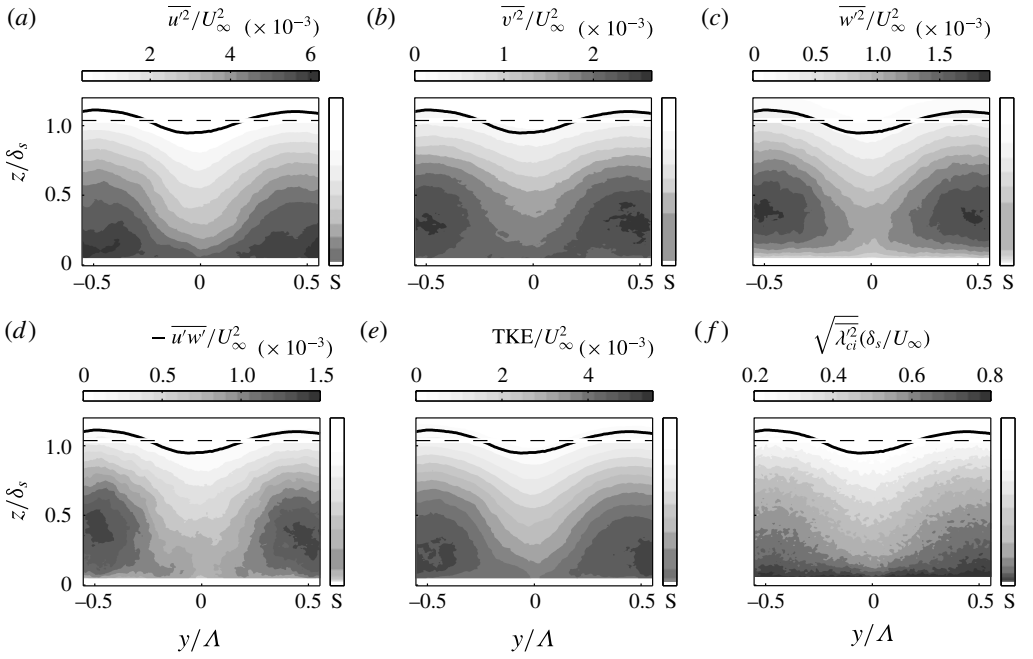


FIGURE 10. Contours of (*a–c*) streamwise, spanwise and wall-normal Reynolds stresses; (*d*,*e*) Reynolds shear-stress and turbulence kinetic energy; (*f*) root mean square of swirling strength over the C–D riblets. The smooth-wall profiles are included as narrow column axes for comparison.

u' however, the $R_{u'u'}$ profiles more closely resemble the accepted smooth-wall result. Nonetheless, no collapse is observed between any of the compared profiles. The average width of the streamwise turbulent events are noticeably narrower over the converging than the diverging region at this locally normalised wall height. From this observation we can see that the C–D riblets alter the instantaneous flow coherence beyond simply imposing a spanwise periodicity. We will further highlight this structural flow modification in § 5 from an instantaneous flow example. For the remainder of this paper, we will only consider the fluctuation about the local mean u_i' to analyse how the convecting turbulence has been altered by the C–D riblets.

4.3. *Reynolds stresses and turbulence kinetic energy distribution*

The distributions of Reynolds normal stresses for the current experiment are displayed in figure 10(*a–c*). The corresponding profiles for the smooth-wall base case are also displayed to the immediate right of each axis, labelled 'S'. The pronounced spanwise variation is clearly apparent in all Reynolds stress components, where the converging (higher wall-drag) region experiences much stronger Reynolds fluctuations compared to the diverging region and the smooth-wall base case. The same behaviour was previously shown by Nugroho *et al.* (2013) over the same type of riblets for the streamwise fluctuating component. The increased magnitude in all turbulence intensities over the converging region clearly suggests that more energetic turbulent events occur in these regions. Figures 10(*d*) and 10(*e*) display the distribution of Reynolds shear stress (RSS) $-\overline{u'w'}$ and the turbulence kinetic energy

https://doi.org/10.1017/jfm.2016.879 Published online by Cambridge University Press

(TKE) respectively, where TKE $= (\overline{u'^2} + \overline{v'^2} + \overline{w'^2})/2$. The spanwise periodicity in both statistics is certainly expected. Both RSS and TKE are much higher over the converging region (higher wall drag) throughout the boundary layer, compared to over the diverging (lower wall-drag) region. Regions of elevated RSS and TKE are also observed experimentally by Barros & Christensen (2014) over complex heterogeneous roughness, where the most energetic locations coincide with the regions of lowered mean streamwise velocity, similar to what occurs over the C–D riblets. Finally, the root mean square of two-dimensional swirling strength λ_{ci} (described in Adrian, Christensen & Liu 2000*a*) is displayed in figure 10(*f*). This figure highlights the more frequent occurrence of intense small-scale turbulence over the converging region, which might indicate that the very-large-scale low-speed events that carry these small-scale vortical motions are preferentially arranged over the converging region.

5. Instantaneous flow structures

Figure 11(*a*) shows an example instantaneous streamwise velocity field u over the C–D riblets. The figure highlights the most prominent feature in the u fields, which is the tall eruption of low-speed fluid over the converging regions. Since this distinct event is observed in almost all instantaneous fields, it results in a strong periodicity in the mean streamwise velocity U. There are rare instances where these eruption events exceed the wall-normal domain of the current measurement, but these events do not affect the single-point statistic results presented in the previous sections. Further visual inspection of the u snapshots reveals that these z-extended regions of low streamwise momentum tend to be tipped over transversely in the outer layer, which is also evidenced in figure 7.

The corresponding large-scale (filtered) in-plane velocities v_f and w_f are plotted in figure 11(*b*). These vectors are filtered using a Gaussian kernel with the size of $0.25 \times 0.25\delta_s$ and standard deviation of 2. The vector grid has also been down-sampled for clarity of presentation. Several large-scale vortical motions can be distinguished in the figure, and the centre of several events are marked by the $\otimes$ symbols (markers are also drawn in figure 11*c*). Note that these streamwise vortices are not the hairpin vortex signatures which are the typical small-scale features as mentioned by Adrian *et al.* (2000*b*), Tomkins & Adrian (2003), Hutchins, Hambleton & Marusic (2005). The large-scale filter kernel employed here would have attenuated these small swirling events, leaving only any residual large-scale tendency. Groups of the same sign swirling events however, can still manifest in these larger-scale rotations. These large-scale streamwise vortices can also be observed instantaneously in the smooth-wall flow fields as naturally occurring unstable motions, but with less magnitude and no preferred spanwise location. However, the directional pattern over the C–D riblets seems to have enhanced the frequency and magnitude of this motion so that it appears in many realisations with a preferred orientation. At $z/\delta = 0.5$ for example, positive large swirling motions that occur in the region $0 < y/\Lambda < 0.5$ are statistically $\sim$16 % stronger than those over the smooth wall. When comparing these instantaneous roll modes to the mean counter-rotating secondary flow shown in figure 6, one can deduce several major differences. Firstly, the diameters of the instantaneous motions are on average smaller than those found in the mean secondary flow that fills the entire boundary layer. Secondly, the centres of these motions do not always occur at $z/\delta_s \approx 0.3$ where the centres of the mean secondary flow appears, and they also tend to wander in the transverse direction. Furthermore, in

https://doi.org/10.1017/jfm.2016.879 Published online by Cambridge University Press

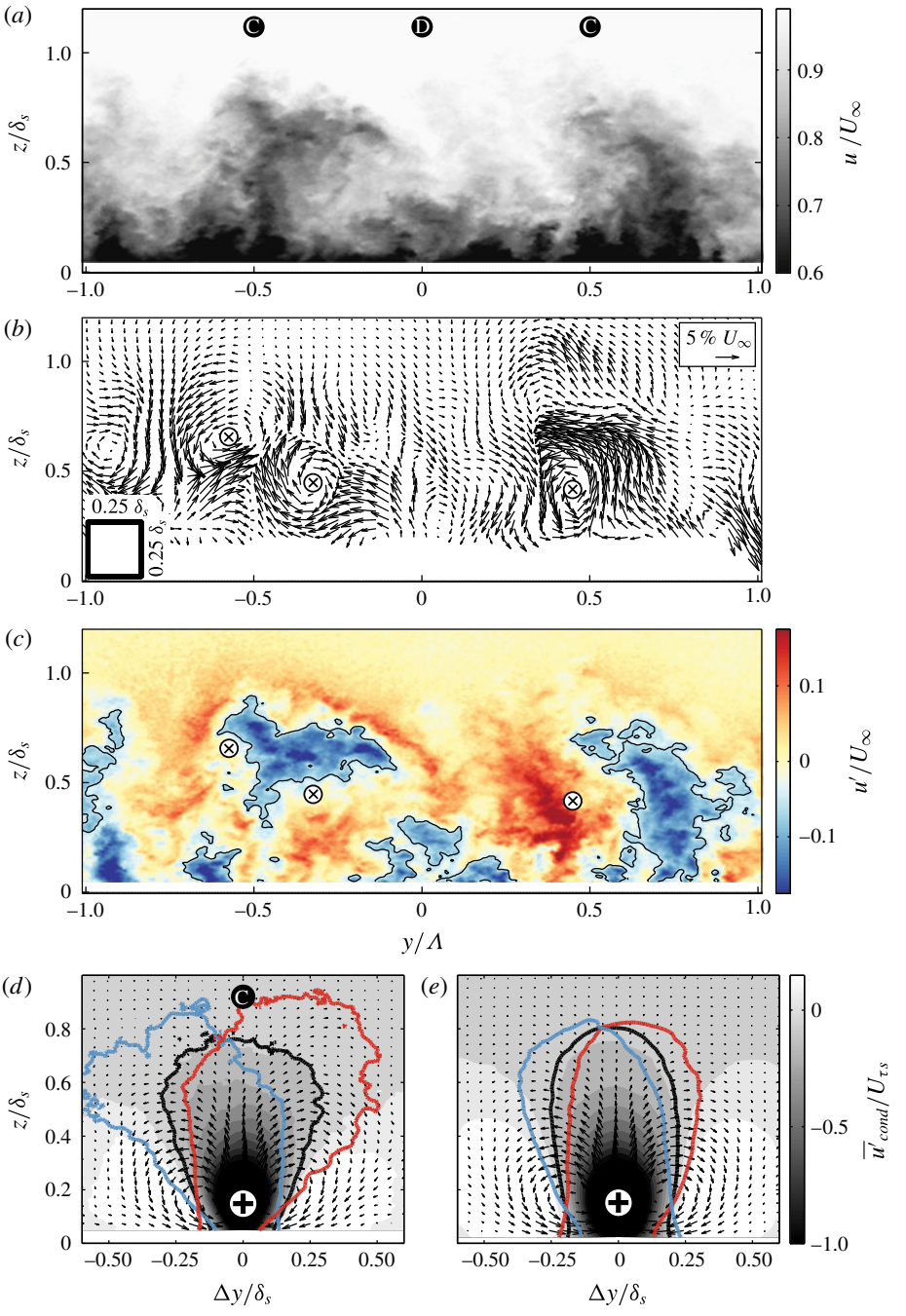


FIGURE 11. Representative example of instantaneous flow over the C–D riblets. (*a*) Total streamwise velocity u. (*b*) The filtered in-plane total velocity v_f and w_f, marker $\otimes$ indicates the centre of the streamwise vortices. (*c*) Streamwise Reynolds fluctuation u', black contour lines indicate $u' = 0.1U_\infty$. (*d*) Conditional-average field over converging line and (*e*) smooth-wall. $+$ symbols indicate the reference point at $z_{ref}/\delta_s = 0.15$. Solid lines indicate contour of $\overline{u'}_{cond} = -0.05U_{\tau s}$. No spanwise fluctuation v' condition (−); $v' < 0$ (−, blue); $v' > 0$ (−, red).

https://doi.org/10.1017/jfm.2016.879 Published online by Cambridge University Press

many instances larger streamwise vortices appear to be one sided within adjacent converging regions. This non-symmetrical behaviour will be further described in § 6. Hence, contrary to the view afforded from the mean statistics (Nugroho *et al.* 2013), it can be concluded that these secondary flows happen intermittently with a multitude of length scales, frequencies and magnitudes, such that the δ-filling roll modes only exist in a time-average sense and are in fact a superposition of stronger individual streamwise vortices. Accordingly, the weakness of the mean roll modes could be somewhat misleading, since instantaneously the picture is one of much stronger individual events induced by the C–D texture.

The turbulence/temporal fluctuation u' of the same instance is displayed in figure 11(*c*). In the cross-stream view, the dominant features in these fields are the large plumes of low streamwise momentum ejecting from the wall, as observed previously by Hutchins *et al.* (2005) in their sPIV measurement in inclined planes (45° and 135° from x-axis) over the smooth wall. As mentioned in § 4.2, removing the local U from this spanwise periodic flow reduces the magnitude of the fluctuations (i.e. the values become less negative near the converging, and less positive near the diverging) especially closer to the riblets surface. Therefore, the negative u' structures can sometimes be seen to be detached from the wall as depicted by the structure at $y/\Lambda = -0.5$. In non-homogeneous flows, subtracting the local mean from the total velocity essentially eliminates the stationary (time-average) spatial variation from the field. Therefore, for flows with less intense spatial heterogeneity such as over the realistic roughness analysed by Barros & Christensen (2014), the instantaneous Reynolds fluctuation field u' will closely resemble the smooth-wall fluctuation field. Over the C–D riblets however, interesting features emerge from careful examination of the flow structures. The ejected low-momentum regions are typically 'curled' either clockwise or anticlockwise depending on their relative spanwise position over the riblets. This behaviour is highlighted by the contour lines of $u' = -0.1U_\infty$ above the converging regions in figure 11(*c*). This large-scale curving behaviour can happen simultaneously in both directions similar to the feature above $y/\Lambda = -0.5$, or more frequently as a one-sided tendency similar to the feature above $y/\Lambda \approx 0.5$ (another example can be seen in figure 7). The markers $\otimes$ also highlight the association between these inclined plumes to the large-scale instantaneous streamwise vortices.

To statistically assess the behaviour of these deformed low-momentum eruptions, we perform conditional averaging over the converging lines at $z_{ref}/\delta_s = 0.15$. The condition is based on the large-scale (filtered) streamwise velocity fluctuation u'_f, which is obtained by convolving the u' field with the same Gaussian kernel used in figure 11(*b*). The unfiltered u' fields are then averaged when $u'_f(\text{converging}, z_{ref}) < -U_{\tau s}$. Here the filter size and the velocity threshold are arbitrarily chosen to represent a large-scale event with considerable energy, and the key results presented are not greatly altered by changes to these values. The result of this conditional averaging is shown in figure 11(*d*), where the grey background colour shows the averaged streamwise fluctuation $\overline{u'}_{cond}$ and the black contour line indicates $\overline{u'}_{cond} = -0.05U_{\tau s}$. The conditional-average field over the smooth wall is also compared in figure 11(*e*). Note that the smooth-wall average structure attains slightly better convergence since the samples can be taken across the entire homogeneous spanwise domain, whereas over the riblets we condition it above the converging lines at $y/\Lambda = \pm 0.5$. Similar to cross-stream observations by Hutchins *et al.* (2005), the average low-momentum region (darker colour) over the smooth wall is flanked by high-momentum regions (lighter colour). The superimposed in-plane conditional vectors also indicate the mean vortical motion that accompanies the low-speed upwash event. These naturally

https://doi.org/10.1017/jfm.2016.879 Published online by Cambridge University Press

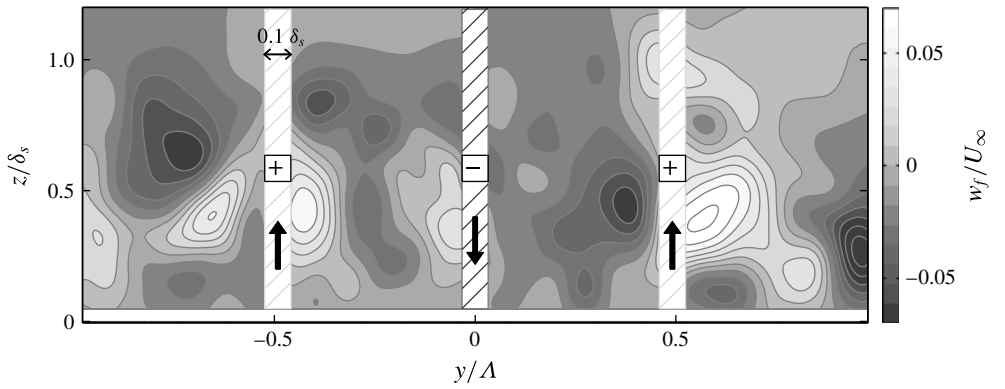


FIGURE 12. The corresponding filtered wall-normal velocity field w_f of the example displayed in figure 11. The hatched regions show the area where w_f is averaged to determine the instantaneous common flow direction within one C–D wavelength.

occurring behaviours are also observed in the conditional field over the converging region. Comparing the width of the contour however (see the black lines), reveals the narrower structure closer to the wall but noticeably wider further from the wall. Extra caution needs to be taken while interpreting the appearance of an average structure, since the observed shape can simply be the resultant statistical shape due to the superposition of several different events. To overcome this issue, we further divide the above conditional fields using the sign of the large-scale spanwise velocity fluctuation v'_f at the condition point. The same sorting is also done on the smooth-wall field for comparison. The red contour line in figure 11(*d*,*e*) indicates the $\overline{u'}_{cond} = -0.05U_{\tau s}$ contour that has positive spanwise velocity $+v'$, and the blue contour indicates the other half that has $-v'$. By sorting in this manner, the average structures over the C–D riblets clearly resemble the left/right leaning low-momentum features observed instantaneously in figure 11(*b*), highlighting their dominance within the flow field. Though this left/right leaning tendency is also weakly observed for the smooth-wall conditional averages in figure 11(*e*), it is much less pronounced than that above the riblets.

6. A closer look at the time-average secondary flow

It appears from figure 11 that the low-momentum regions above the converging part of the riblets undergo a lateral instability accompanied by predominantly one-sided arrangements of large-scale vortical motions. This suggests that the counter-rotating mode observed in the time-average view of figure 6 is not representative of the instantaneous vortex arrangement induced by the surface texture. Here we attempt to quantify this time-variant behaviour. Again, we will utilise conditional-averaging technique to establish the fractional time when the flow instantaneously exhibits a large counter-rotating motion within one C–D wavelength. Note that conditional averaging will essentially enforce a flow pattern that we are querying. Hence, careful interpretation is necessary, and our emphasis is on the proportion of snapshots that resemble the conditional features.

The velocity frames are sorted based on the instantaneous vertical velocity above the C–D-C regions. This process is illustrated in figure 12, where it shows the filtered wall-normal velocity w_f corresponding to the example given in figure 11.

https://doi.org/10.1017/jfm.2016.879 Published online by Cambridge University Press

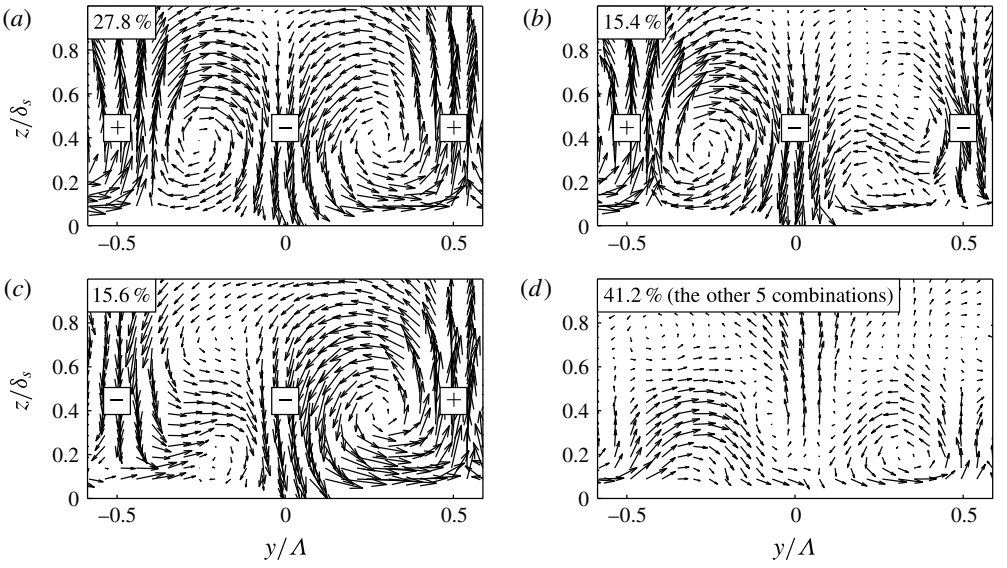


FIGURE 13. Conditional-average velocity vectors, sorted based on the sign (direction) of the vertical common flow above $y/\Lambda = -0.5, 0, 0.5$. (*a*) Conditional vectors when average-w_f are $+, -, +$. (*b*,*c*) Conditional vectors when average-w_f are $+, -, -$ and $-, -, +$ respectively. (*d*) Conditional vectors for the rest of the combinations. Figure is drawn to scale with figure 6.

This filtered component w_f is averaged within a spanwise width of $0.1\delta_s$ (hatched region), to determine the instantaneous sign of the vertical flow in these three regions. In this particular example, the result is up-down-up since the resulting average is $+, -, +$. All frames are then sorted based on this three-sign combination, giving 2^3 possibilities. From this, conditionally averaged views of the cross-flow vectors v and w can be produced for each combination. Note that if all combinations are included, the conditional average will return the time-average secondary flow shown by the vectors in figure 6. Figure 13(*a*) displays the average in-plane velocities when the vertical signs over $y/\Lambda = -0.5, 0, 0.5$ are $+, -, +$ respectively. One can quickly notice that this pattern resembles the mean secondary flow, with the left side ($-0.5 < y/\Lambda < 0$) exhibiting a δ-filling negative streamwise vortex and the right side ($0 < y/\Lambda < 0.5$) showing the positive. Interestingly, this pattern is observed only for 27.8 % of the seven thousand acquired realisations. Figures 13(*b*) and 13(*c*), where the average w_f are $+, -, -$ and $-, -, +$ respectively, also confirm that one-sided large-scale rotational motions occur more frequently (31 % of realisations) compared to the counter-rotating case shown in figure 13(*a*).

Due to the forced condition, figure 13(*a–c*) displays at least one large-scale streamwise roll modes with the expected rotational sense. Figure 13(*d*) however, contains the other five combinations (i.e. $+, +, +$; $-, -, -$; $-, +, -$; $-, +, +$; $+, +, -$). These lower percentage patterns are not individually plotted here for brevity. The average vortex pattern in these other combinations will either show the large-scale motions that turn the opposite to the time-average secondary flow, or consist of smaller rotational events. Again, these patterns are certainly enforced by the given condition events. However, it is definitely striking that these other five combinations (where each of the conditionally averaged field in no way resembles

https://doi.org/10.1017/jfm.2016.879 Published online by Cambridge University Press

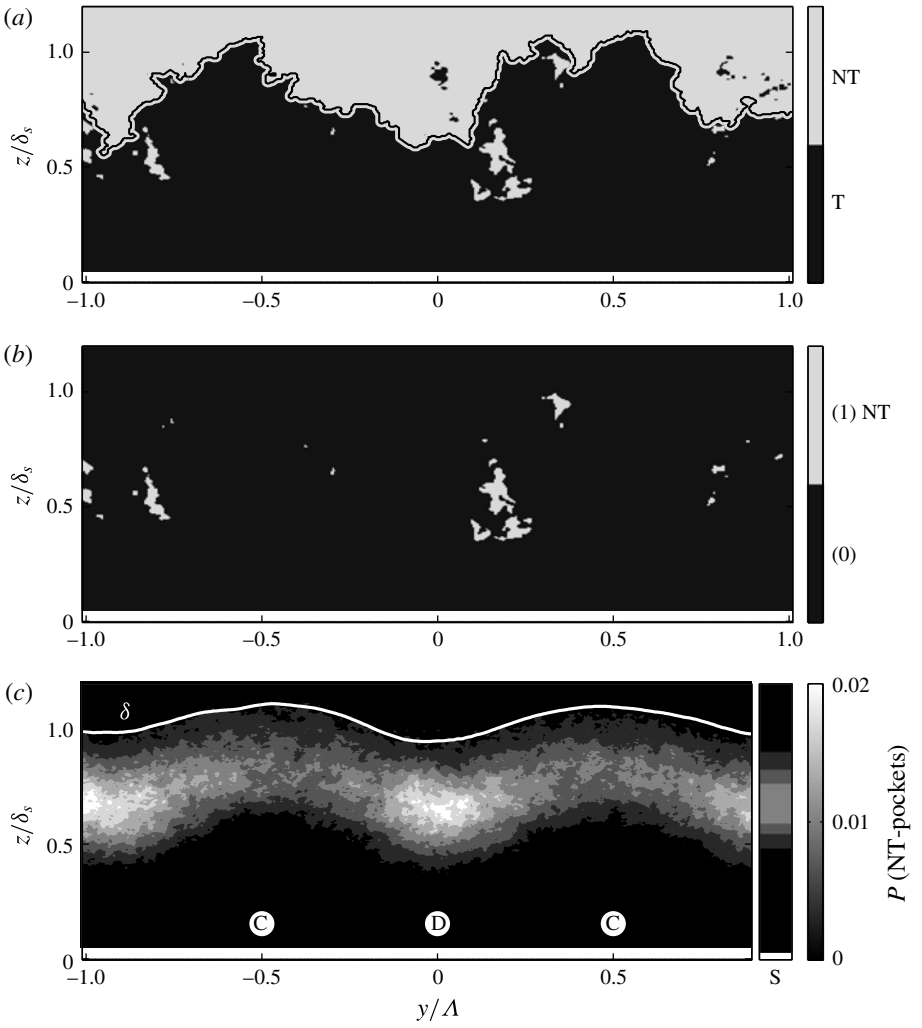


FIGURE 14. (*a*) Example of instantaneous field separated into turbulent/non-turbulent regions, with the interface outline superimposed. (*b*) The corresponding binary field of the non-turbulent pockets (assigned to be 1) and the rest of the field (assigned to be 0). (*c*) Probability of the non-turbulent pockets occurrence. The smooth-wall profile is included as a column axis.

the time-averaged secondary flow) comprise 41.5 % of the total snapshots. The overall conclusion here would be that the large vortical events that give rise to the time-average secondary flow are to some extent intermittent in time (possibly also in the x-direction), and that the time-averaging process has masked the often much stronger instantaneous large-scale roll modes that are induced by the surface texture.

7. The effect of C–D riblets in the intermittent flow region

Over the diverging part of the riblets (where the mean common flow down occurs), regions of fast moving fluid with a streamwise velocity approximately equal to the free-stream value are often observed deep within the boundary layer. These regions occur below the turbulent/non-turbulent (T/NT) 'interface outline' defined by

https://doi.org/10.1017/jfm.2016.879 Published online by Cambridge University Press

Chauhan *et al.* (2014), and typically reside underneath the leaning low-momentum eruptions described in § 5. To illustrate this observation, figure 14(*a*) presents a realisation where the field has been separated into the turbulent (darker colour) and non-turbulent/free-stream (lighter colour) regions. These T/NT regions are identified using the kinetic-energy criteria of Chauhan *et al.* (2014), and the aforementioned interface outline is also highlighted. In this example, many 'pockets' of non-turbulent fluid (i.e. patches of small non-turbulent area which are fully encapsulated within the turbulent region) are present in the field of view. These pockets represent the potential flow regions that are perhaps drawn into the boundary layer by the large instantaneous motion discussed in § 5. The binary figure 14(*b*) highlights the occurrence of these NT pockets, where they are assigned the value 1 and the rest of the field are assigned 0. Viewing through multiple realisations, one can see a clear trend that patches of NT fluid often occur nominally above the diverging part of the riblets, although their locations vary slightly from frame to frame. This observation is then confirmed statistically by looking at the spatial probability P of the NT-pocket occurrence, which is presented in figure 14(*c*). The probability is calculated by ensemble averaging the binary images of figure 14(*b*), and the result reveals a strong spanwise periodicity over the C–D riblets. The distribution of the smooth-wall base case is also included as the narrow axis immediately to the right, and labelled 'S'. Over the converging region, the NT pockets seem to occur with similar frequency to the smooth-wall case. Over the diverging region however, this phenomena occurs twice as often. The observed large-scale engulfment of free-stream flow by the modified boundary layer might suggest that a certain degree of 'forced mixing' (Schubauer & Spangenberg 1960) has been imposed. This process will extract free-stream momentum towards the wall and facilitate the movement of the less energetic fluids. This possible mixing property opens a potential of using C–D riblets as a tool to delay boundary layer separation and to increase heat transfer without adding a significant amount of parasitic form drag.

8. Summary

A stereoscopic PIV experiment has been performed in a turbulent boundary layer over a converging–diverging riblet surface. The results and relevant discussions presented in this paper are summarised as follows,

(i) We categorise surface roughness based on their local C_f isotropy and their drag homogeneity. The herringbone pattern discussed here is considered anisotropic (directional)-heterogeneous roughness. Although time-averaged secondary flows are present for both the isotropic and anisotropic spanwise heterogeneous categories, several noted differences (such as the surface characteristics and the secondary flow orientation) suggest that different mechanisms may be responsible for their generation.

(ii) The spanwise periodicity over the C–D riblets is pronounced, to the extent that the boundary layer thickness is locally altered. Accompanying this periodicity are mean counter-rotating roll modes. The orientation of these cellular roll modes can be inferred from assumption that upward/downward motions occur above region of flow convergence/divergence respectively. Strong spanwise variations are also observed in all Reynolds stress and the turbulence kinetic energy fields, where increased quantities are always observed above the converging regions. All second-order statistics are lower over the diverging region compared to the converging and the smooth-wall case.

https://doi.org/10.1017/jfm.2016.879 Published online by Cambridge University Press

(iii) Instantaneous analysis on the streamwise velocity fields reveal the consistent occurrence low momentum eruptions above the converging regions, as suggested by the time-average field. These large-scale events however, are often observed to be leaning in the transverse direction, and accompanied by large scale often asymmetric rotational motions. The conditional-average results reveal the dominance of these leaning structures in the flow field. This suggests that the large-scale low momentum regions that occur over the converging regions undergo a lateral instability that is stronger than that observed on the naturally occurring low momentum regions.

(iv) By employing a conditional sorting technique, we show that the instantaneous in-plane rotational motions resemble their time-average in-plane vectors for only 28 % of the fractional time. This observation perhaps offer an explanation regarding why this fully modified boundary layer is only accompanied by a very weak time-averaged 'residual' secondary flow. The present results suggest that the time-averaged V and W interpreted as mean secondary flows are perhaps an artefact of the averaging process arising from superpositions of much stronger turbulent events.

(v) Large-scale free-stream engulfing behaviour is often observed associated with the common flow down tendency of the secondary flows. These motions cause a more frequent occurrence of free-stream pockets above the diverging region compared to the smooth-wall flow (without noticeable changes over the converging region). This observation might indicate an increase in flow mixing over the converging–diverging riblets.

Acknowledgements

The authors wish to thank the Australian Research Council for the financial support of this research. K.T.C., J. B. and G.P. gratefully acknowledge the support of the Air Force Office of Scientific Research under grant nos FA9550-10-1-0372 and FA9550-14-1-0101 (Dr D. Smith, Program Manager).

REFERENCES

ACHARYA, M., BORNSTEIN, J. & ESCUDIER, M. P. 1986 Turbulent boundary layers on rough surfaces. *Exp. Fluids* **4** (1), 33–47.

ADRIAN, R. J., CHRISTENSEN, K. T. & LIU, Z. C. 2000*a* Analysis and interpretation of instantaneous turbulent velocity fields. *Exp. Fluids* **29** (3), 275–290.

ADRIAN, R. J., MEINHART, C. D. & TOMKINS, C. D. 2000*b* Vortex organization in the outer region of the turbulent boundary layer. *J. Fluid Mech.* **422**, 1–54.

DEL ÁLAMO, J. C., JIMÉNEZ, J., ZANDONADE, P. & MOSER, R. D. 2006 Self-similar vortex clusters in the turbulent logarithmic region. *J. Fluid Mech.* **561**, 329–358.

ANDERS, J. B. 1990 Outer-layer manipulators for turbulent drag reduction. *Visc. Drag Reduc. Boundary Layers* **123**, 263–284.

ANDERSON, W., BARROS, J. M., CHRISTENSEN, K. T. & AWASTHI, A. 2015 Numerical and experimental study of mechanisms responsible for turbulent secondary flows in boundary layer flows over spanwise heterogeneous roughness. *J. Fluid Mech.* **768**, 316–347.

BARROS, J. M. & CHRISTENSEN, K. T. 2014 Observations of turbulent secondary flows in a rough-wall boundary layer. *J. Fluid Mech.* **748**, R1.

BECHERT, D. W. & BARTENWERFER, M. 1989 The viscous flow on surfaces with longitudinal ribs. *J. Fluid Mech.* **206**, 105–129.

https://doi.org/10.1017/jfm.2016.879 Published online by Cambridge University Press

BECHERT, D. W., BRUSE, M. & HAGE, W. 2000 Experiments with three-dimensional riblets as an idealized model of shark skin. *Exp. Fluids* **28** (5), 403–412.

BECHERT, D. W., BRUSE, M., HAGE, W., DER HOEVEN, J. G. T. VAN & HOPPE, G. 1997 Experiments on drag-reducing surfaces and their optimization with an adjustable geometry. *J. Fluid Mech.* **338**, 59–87.

CHAN, L., MACDONALD, M., CHUNG, D., HUTCHINS, N. & OOI, A. 2015 A systematic investigation of roughness height and wavelength in turbulent pipe flow in the transitionally rough regime. *J. Fluid Mech.* **771**, 743–777.

CHAUHAN, K., PHILIP, J., DE SILVA, C. M., HUTCHINS, N. & MARUSIC, I. 2014 The turbulent/non-turbulent interface and entrainment in a boundary layer. *J. Fluid Mech.* **742**, 119–151.

CHEN, H., RAO, F., SHANG, X., ZHANG, D. & HAGIWARA, I. 2014 Flow over bio-inspired 3d herringbone wall riblets. *Exp. Fluids* **55** (3), 1–7.

CHOI, K. S. 1989 Near wall structure of turbulent boundary layer with riblets. *J. Fluid Mech.* **208**, 417–458.

COCEAL, O., THOMAS, T. G., CASTRO, I. P. & BELCHER, S. E. 2006 Mean flow and turbulence statistics over groups of urban-like cubical obstacles. *Boundary-Layer Meteorol.* **121** (3), 491–519.

EITEL-AMOR, G., ÖRLÜ, R. & SCHLATTER, P. 2014 Simulation and validation of a spatially evolving turbulent boundary layer up to $Re_\theta = 8300$. *Intl J. Heat Fluid Flow* **47**, 57–69.

FINNIGAN, J. J. 2000 Turbulence in plant canopies. *Annu. Rev. Fluid Mech.* **32** (1), 519–571.

FLACK, K. A. & SCHULTZ, M. P. 2010 Review of hydraulic roughness scales in the fully rough regime. *J. Fluids Engng* **132** (4), 041203.

FLACK, K. A., SCHULTZ, M. P. & SHAPIRO, T. A. 2005 Experimental support for Townsend's Reynolds number similarity hypothesis on rough walls. *Phys. Fluids* **17** (3), 035102.

GARCÍA-MAYORAL, R. & JIMÉNEZ, J. 2011 Hydrodynamic stability and breakdown of the viscous regime over riblets. *J. Fluid Mech.* **678**, 317–347.

GRANVILLE, P. S. 1958 The frictional resistance and turbulent boundary layer of rough surfaces. *Tech. Rep.* 1024.

HINZE, J. 1967 Secondary currents in wall turbulence. *Phys. Fluids (Suppl.)* **10**, S122–S125.

HINZE, J. O. 1973 Experimental investigation on secondary currents in the turbulent flow through a straight conduit. *Appl. Sci. Res.* **28** (1), 453–465.

HUTCHINS, N., HAMBLETON, W. T. & MARUSIC, I. 2005 Inclined cross-stream stereo particle image velocimetry measurements in turbulent boundary layers. *J. Fluid Mech.* **541**, 21–54.

HUTCHINS, N. & MARUSIC, I. 2007 Evidence of very long meandering features in the logarithmic region of turbulent boundary layers. *J. Fluid Mech.* **579**, 1–28.

JIMÉNEZ, J. 2004 Turbulent flows over rough walls. *Annu. Rev. Fluid Mech.* **36**, 173–196.

KAMRIN, K., BAZANT, M. Z. & STONE, H. A. 2010 Effective slip boundary conditions for arbitrary periodic surfaces: the surface mobility tensor. *J. Fluid Mech.* **658**, 409–437.

KIM, K. C. & ADRIAN, R. J. 1999 Very large-scale motion in the outer layer. *Phys. Fluids* **11** (2), 417–422.

KOELTZSCH, K., DINKELACKER, A. & GRUNDMANN, R. 2002 Flow over convergent and divergent wall riblets. *Exp. Fluids* **33** (2), 346–350.

LEE, J. H., KEVIN, MONTY, J. P. & HUTCHINS, N. 2016 Validating under-resolved turbulence intensities for PIV experiments in canonical wall-bounded turbulence. *Exp. Fluids*.

LUCHINI, P., MANZO, F. & POZZI, A. 1991 Resistance of a grooved surface to parallel flow and cross-flow. *J. Fluid Mech.* **228**, 87–109.

MEJIA-ALVAREZ, R. & CHRISTENSEN, K. T. 2013 Wall-parallel stereo particle-image velocimetry measurements in the roughness sublayer of turbulent flow overlying highly irregular roughness. *Phys. Fluids* **25** (1), 115109.

MONTY, J. P., STEWART, J. A., WILLIAMS, R. C. & CHONG, M. S. 2007 Large-scale features in turbulent pipe and channel flows. *J. Fluid Mech.* **589**, 147–156.

MOODY, L. F. 1944 Friction factors for pipe flow. *Trans. ASME* **66** (8), 671–684.

NAPOLI, E., ARMENIO, V. & MARCHIS, M. D. 2008 The effect of the slope of irregularly distributed roughness elements on turbulent wall-bounded flows. *J. Fluid Mech.* **613**, 385–394.

https://doi.org/10.1017/jfm.2016.879 Published online by Cambridge University Press

NUGROHO, B., GNANAMANICKAM, E. P., KEVIN, MONTY, J. P. & HUTCHINS, N. 2014 Roll-modes generated in turbulent boundary layers with passive surface modifications. *AIAA paper*.

NUGROHO, B., HUTCHINS, N. & MONTY, J. P. 2013 Large-scale spanwise periodicity in a turbulent boundary layer induced by highly ordered and directional surface roughness. *Intl J. Heat Fluid Flow* **41**, 90–102.

PERRY, A. E. & LI, J. D. 1990 Experimental support for the attached-eddy hypothesis in zero-pressure gradient turbulent boundary layers. *J. Fluid Mech.* **218**, 405–438.

PERRY, A. E., SCHOFIELD, W. H. & JOUBERT, P. N. 1969 Rough wall turbulent boundary layers. *J. Fluid Mech.* **37** (02), 383–413.

PRANDTL, L. & SCHLICHTING, H. 1955 The resistance law for rough plates, translated by P. S. Granville. *Tech. Rep.* 258.

RAUPACH, M. R. & SHAW, R. H. 1982 Averaging procedures for flow within vegetation canopies. *Boundary-Layer Meteorol.* **22** (1), 79–90.

SCHUBAUER, G. B. & SPANGENBERG, W. G. 1960 Forced mixing in boundary layers. *J. Fluid Mech.* **8**, 10–32.

SHOCKLING, M. A., ALLEN, J. J. & SMITS, A. J. 2006 Roughness effects in turbulent pipe flow. *J. Fluid Mech.* **564**, 267–285.

DE SILVA, C. M., GNANAMANICKAM, E. P., ATKINSON, C., BUCHMANN, N. A., HUTCHINS, N., SORIA, J. & MARUSIC, I. 2014 High spatial range velocity measurements in high Reynolds number turbulent boundary layer. *Phys. Fluids* **26** (2), 025117.

SOLOFF, S. M., ADRIAN, R. J. & LIU, Z. C. 1997 Distortion compensation for generalized stereoscopic particle image velocimetry. *Meas. Sci. Technol.* **8** (12), 1441–1454.

TOMKINS, C. D. & ADRIAN, R. J. 2003 Spanwise structure and scale growth in turbulent boundary layers. *J. Fluid Mech.* **490**, 37–74.

VANDERWEL, C. & GANAPATHISUBRAMANI, B. 2015 Effects of spanwise spacing on large-scale secondary flows in rough-wall turbulent boundary layers. *J. Fluid Mech.* **774**, R2.

VERMAAS, D. A., UIJTTEWAAL, W. S. J. & HOITINK, A. J. F. 2011 Lateral transfer of streamwise momentum caused by a roughness transition across a shallow channel. *Water Resour. Res.* **47** (2), W02530.

VOLINO, R. J., SCHULTZ, M. P. & FLACK, K. A. 2009 Turbulence structure in a boundary layer with two-dimensional roughness. *J. Fluid Mech.* **635**, 75–101.

WALSH, M. J. 1990 Effect of detailed surface geometry on riblet drag reduction performance. *J. Aircraft.* **27** (6), 572–573.

WANG, Z. Q. & CHENG, N. S. 2006 Time-mean structure of secondary flows in open channel with longitudinal bedforms. *Adv. Water Resour.* **29** (11), 521–542.

WILLINGHAM, D., ANDERSON, W., CHRISTENSEN, K. T. & BARROS, J. M. 2014 Turbulent boundary layer flow over transverse aerodynamic roughness transitions: induced mixing and flow characterization. *Phys. Fluids* **26** (2), 025117.

WU, Y. & CHRISTENSEN, K. T. 2010 Spatial structure of a turbulent boundary layer with irregular surface roughness. *J. Fluid Mech.* **655**, 380–418.

https://doi.org/10.1017/jfm.2016.879 Published online by Cambridge University Press